

A mechanism for the recently increased interdecadal variability of the Silk Road Pattern

Article

Published Version

Stephan, C. C., Klingaman, N. P. ORCID: <https://orcid.org/0000-0002-2927-9303> and Turner, A. G. ORCID: <https://orcid.org/0000-0002-0642-6876> (2019) A mechanism for the recently increased interdecadal variability of the Silk Road Pattern. *Journal of Climate*, 32. pp. 717-736. ISSN 1520-0442 doi: 10.1175/JCLI-D-18-0405.1 Available at <https://centaur.reading.ac.uk/80821/>

It is advisable to refer to the publisher's version if you intend to cite from the work. See [Guidance on citing](#).

To link to this article DOI: <http://dx.doi.org/10.1175/JCLI-D-18-0405.1>

Publisher: American Meteorological Society

All outputs in CentAUR are protected by Intellectual Property Rights law, including copyright law. Copyright and IPR is retained by the creators or other copyright holders. Terms and conditions for use of this material are defined in the [End User Agreement](#).

www.reading.ac.uk/centaur

CentAUR

Central Archive at the University of Reading

Reading's research outputs online

A Mechanism for the Recently Increased Interdecadal Variability of the Silk Road Pattern

CLAUDIA CHRISTINE STEPHAN, NICHOLAS P. KLINGAMAN, AND ANDREW G. TURNER

National Centre for Atmospheric Science and Department of Meteorology, University of Reading, Reading, United Kingdom

(Manuscript received 22 June 2018, in final form 10 November 2018)

ABSTRACT

The Silk Road pattern (SRP) teleconnection manifests in summer over Eurasia, where it is associated with substantial temperature and precipitation anomalies. The SRP varies on interannual and decadal scales; reanalyses show an increase in its decadal variability around the mid-1970s. Understanding what drives this decadal variability is particularly important, because contemporary seasonal prediction models struggle to predict the phase of the SRP. Based on analysis of observations and multiple targeted numerical experiments, this study proposes a mechanism for decadal SRP variability. Causal effect network analysis confirms a positive feedback loop between the eastern portion of the SRP pattern and vertical motion over India on synoptic time scales. Anomalies over a larger region of subtropical South Asia can reinforce a background state that projects onto the positive or negative SRP through this mechanism. This effect is isolated and confirmed in targeted numerical simulations. The transition from weak to strong decadal variability in the mid-1970s is consistent with more spatially coherent interannual precipitation variability over subtropical South Asia. Furthermore, results suggest that oceanic variability does not directly force the SRP. Nevertheless, sea surface temperatures in the North Atlantic and the North Pacific may indirectly affect the SRP by modulating South Asian rainfall on decadal time scales.


1. Introduction

The Silk Road pattern (SRP) teleconnection manifests in June–August (JJA), associated with a stationary Rossby wave that is trapped along the subtropical Eurasian jet stream (Lu et al. 2002; Enomoto et al. 2003). Its most prominent features are zonally oriented, geographically anchored anomalies in the upper-tropospheric meridional wind field (Fig. 1a; Lu et al. 2002; Enomoto et al. 2003; Kosaka et al. 2009). Interannual SRP variability (Fig. 1b) is accompanied by substantial regional surface temperature anomalies across Eurasia (green boxes in Fig. 1c; see also Figs. 2a,b; Lu et al. 2002; Wu 2002; Enomoto et al. 2003; Ding and Wang 2005; Huang et al. 2011; Chen and Huang 2012; Saeed et al. 2011; Saeed et al. 2014; Hong and Lu 2016; Wang et al. 2017). However, it is not known what factors modulate the SRP on interannual

(IA) to interdecadal (ID) time scales, or whether there exists the potential for predictability.

The SRP can be interpreted as the Eurasian portion of the summertime circumglobal teleconnection (CGT; Ding and Wang 2005), which over Eurasia has a similar structure to the SRP, but is associated with upper-tropospheric wind anomalies across the entire Northern Hemisphere. The CGT may be excited by tropical Atlantic convection and sea surface temperature (SST) anomalies (Lu et al. 2002) or by convection over the northern Indian Ocean (Chen and Huang 2012). El Niño–Southern Oscillation (ENSO) may modulate the CGT through the impact of ENSO on monsoonal heat sources in the tropics (Ding et al. 2011). This ENSO–CGT relationship has been associated with anomalously strong or weak Indian summer monsoon (ISM) rainfall (Ding and Wang 2005).

Energy conversion through the extraction of available potential energy from the baroclinic Asian jet was shown to be critical for the self-maintenance of the SRP, and for anchoring the strongest vorticity anomalies to the observed preferred locations (Sato and Takahashi 2006; Kosaka et al. 2009; Chen et al. 2013). Another

 Denotes content that is immediately available upon publication as open access.

Corresponding author: Claudia Christine Stephan, c.c.stephan@reading.ac.uk

DOI: 10.1175/JCLI-D-18-0405.1

© 2019 American Meteorological Society. For information regarding reuse of this content and general copyright information, consult the [AMS Copyright Policy](https://www.ametsoc.org/PUBSReuseLicenses) (www.ametsoc.org/PUBSReuseLicenses).

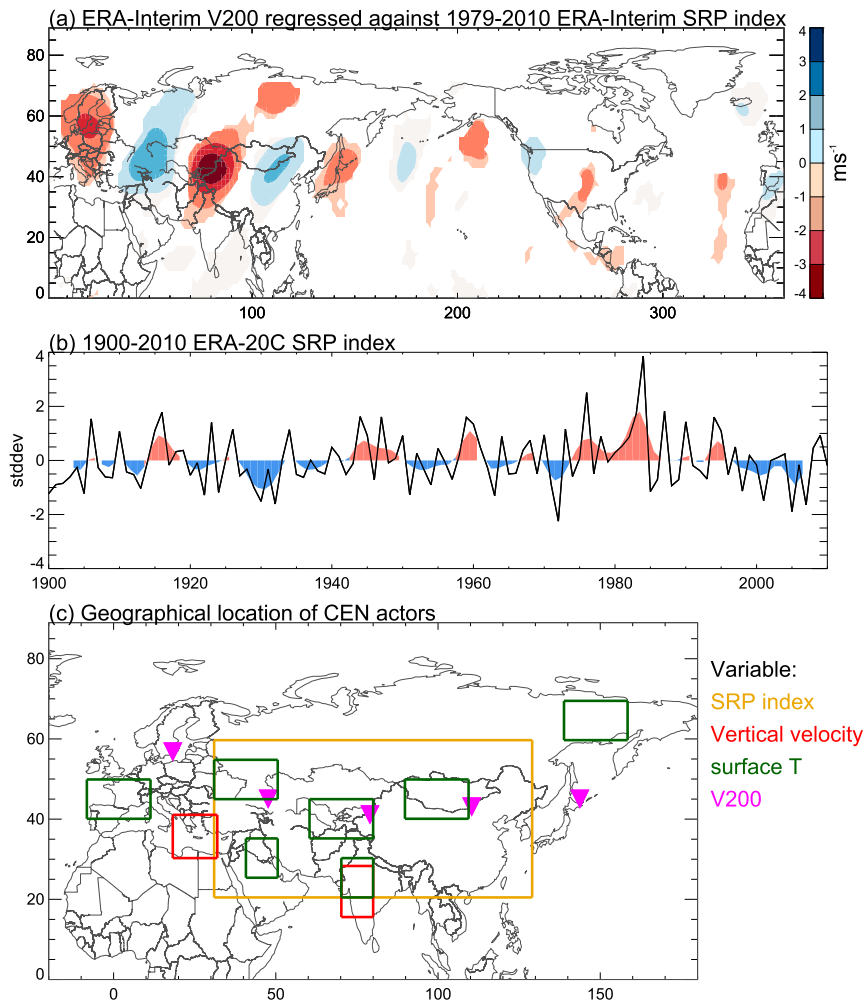


FIG. 1. (a) Regression of ERA-Interim JJA V_{200} against the normalized 1979–2010 ERA-Interim SRP index. (b) 1900–2010 ERA-20C SRP index (black line) and its ID component (blue and red shading). (c) Locations of the CEN actors, which are also listed in Table 2: SRP index (golden box), 500-hPa vertical velocity ω (red boxes), 2-m temperature T (green boxes), and V_{200} (magenta triangles).

proposed mechanism for the self-maintenance is a two-way interaction with the ISM (Ding and Wang 2005): on the one hand, upstream disturbances triggered by barotropic instabilities in the North Atlantic jet exit region can lead to an anomalous upper-level high over western Europe. A secondary anomalous upper-level high over west-central Asia, east of the Caspian Sea, is induced through an eastward-propagating Rossby wave on the subtropical westerly jet. This is associated with stronger convection over northwest India. On the other hand, an anomalous ISM creates a baroclinic circulation northwest of India, which in turn excites an anomalous upper-level west-central Asian high and may trigger additional eastward-propagating Rossby waves (Fig. 15 of Ding and Wang 2005).

Ding and Wang (2007) suggested that this two-way interaction also occurred on intraseasonal scales (see their Fig. 11). Interaction and feedback between extratropical disturbances associated with the SRP and the South Asian monsoon can lead to disastrous meteorological events, such as the 2010 Pakistan flooding and Russian heat wave (Lau and Kim 2012; Kosaka et al. 2012). Processes for monsoon–extratropical circulation interactions, leading to intraseasonal extremes, include midlatitude blocking, Rossby wave breaking, the migration of the monsoon trough, and diabatic forcing from strong convection (Vellore et al. 2016). In August IA SRP variability has been associated with a stronger Bonin high and heat waves over Japan (Enomoto 2004).

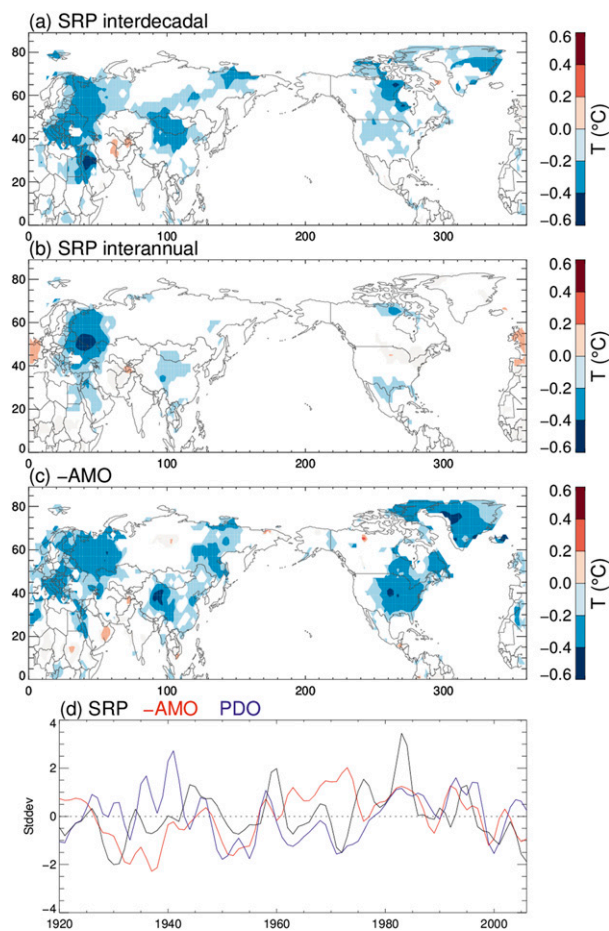


FIG. 2. Regressions of 1920–2006 UDEL 1.5-m temperature against (a) the ID component of the ERA-20C SRP index, (b) the IA component of the SRP index, and (c) the ID component of the AMO index [the AMO sign was flipped to allow for a better comparison with (a) and (b)]. All values shown are significant at the 10% level. All indices were first normalized. (d) The normalized ID SRP, AMO (flipped sign), and PDO indices.

Anomalous convection associated with the ISM affects not only the strength of the eastern portion of the SRP through the west-central Asian high, but also vertical motion over the eastern Mediterranean through the “monsoon–desert mechanism.” Sinking over the eastern Mediterranean and in the west-central Asian high region is associated with the positive phase of the unfiltered SRP (Fig. 3a), the ID SRP (Fig. 3c), and the IA SRP (Fig. 3e). A positive SRP is associated with increased precipitation over India (Figs. 3b,d,f). Compared to unfiltered or IA-filtered (Figs. 3b,f) anomalies, ID precipitation anomalies associated with the SRP cover a larger area of India (Fig. 3d). According to Rodwell and Hoskins (1996), heating associated with the ISM triggers westward-propagating equatorial Rossby waves that induce subsidence over the eastern

Mediterranean through their interaction with the midlatitude westerlies. Tyrlis et al. (2013) analyzed the dynamics of the monsoon–desert mechanism on intra-seasonal scales with an emphasis on the synchronicity and causality of processes over the Mediterranean Sea and the Asian monsoon regions. They confirmed that the eastern Mediterranean is a “passive receiver of the monsoon signal.” Central India (15° – 28° N, 70° – 80° E) and an area over and to the north of the Bay of Bengal (15° – 28° N, 82° – 100° E) were identified as the most important regions for triggering subsidence over the eastern Mediterranean. Tyrlis et al. (2013) argued that heat sources in these regions are relatively efficient generators of Rossby waves, which are able to propagate west because the July 200-hPa zonal winds are weaker at 25° – 30° N than farther south. Such waves are suppressed in easterly or strong westerly flow (Lin et al. 2007; Lin 2009).

The SRP is reproduced as the dominant mode of upper-tropospheric meridional wind variability in those models from phase 3 of the Coupled Model Intercomparison Project (CMIP3) that simulate well the structure of the Eurasian jet (Kosaka et al. 2009). The CGT can also be simulated by a dry nonlinear model forced with global heating derived from monthly observations (Yasui and Watanabe 2010). Coupled seasonal prediction models from the Climate Prediction and Its Application to Society (CliPAS) project (Wang et al. 2009; Lee et al. 2010) initialized on 1 May are also able to produce the SRP’s spatial structure as the leading mode of atmospheric variability, but they cannot reliably predict its phase at monthly to seasonal lead times (Kosaka et al. 2012).

Decadal changes in temperature and precipitation over Eurasia have been associated with SRP-like wave patterns (Zhu et al. 2011; Hong et al. 2017; Piao et al. 2017; Si and Ding 2016). Huang et al. (2015) concluded that the SRP, ISM precipitation, and Atlantic multidecadal oscillation (AMO) contributed to decadal precipitation changes in midlatitude Eurasia. Based on observational and reanalysis data, Wang et al. (2017) reported that the magnitude of the ID SRP variability was substantially smaller before the mid-1970s than after (see also Fig. 1b). They extracted the ID component of the SRP using a low-pass filter and separately analyzed the spatial structures of the ID and residual components. The “ID SRP” had a greater meridional extent than the traditional SRP, with circulation anomalies spreading farther north than in Fig. 1a. Anomalies associated with the ID SRP explained up to 50% of the variance of surface air temperature over eastern Europe, western Asia, and eastern Siberia. However, on IA scales, temperature anomalies in

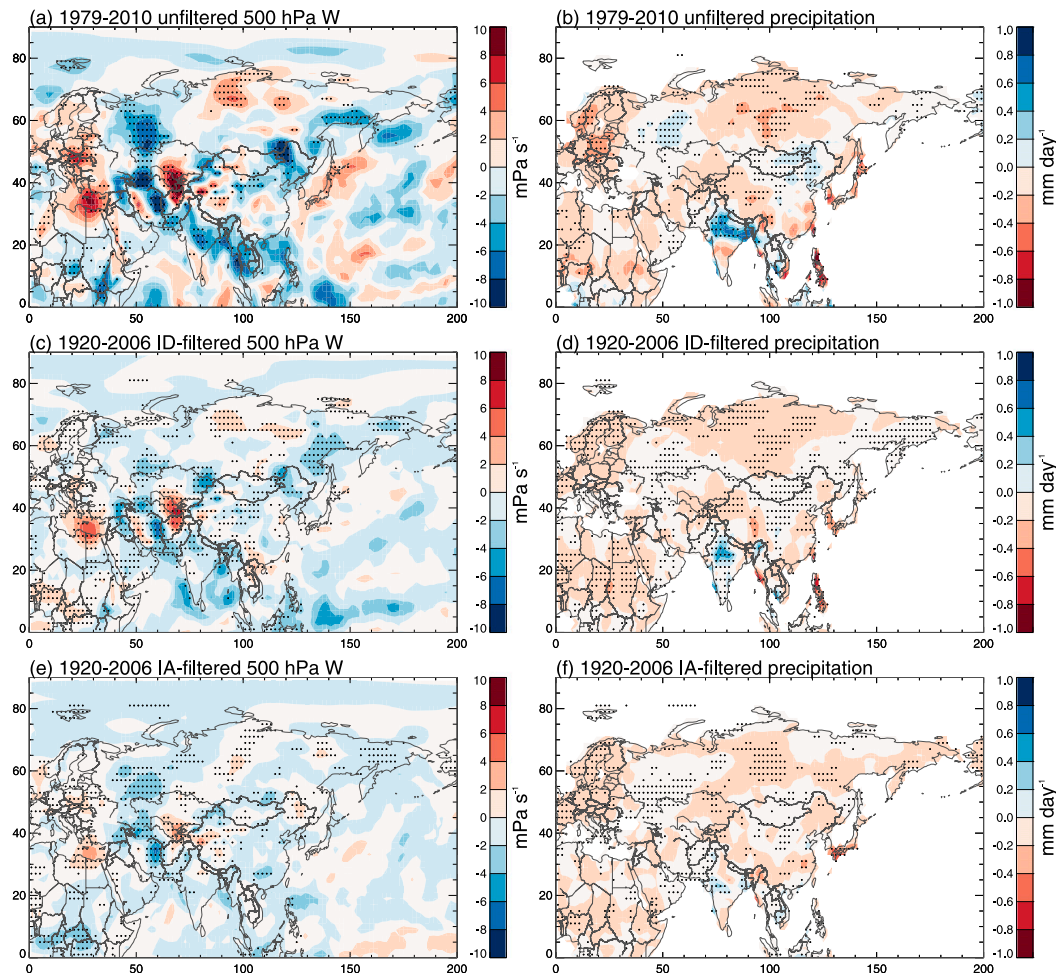


FIG. 3. Regression of (a) 1979–2010 ERA-20C 500-hPa pressure velocity and (b) UDEL precipitation against the normalized 1979–2010 ERA-20C SRP index. Also shown are the regression of 1920–2006 ERA-20C (c), (e) 500-hPa pressure velocity and (d), (f) UDEL precipitation against the (c), (d) ID or (e), (f) IA components of the ERA-20C SRP index. Stippling indicates values that are significant at the 10% level. The 1920–2006 time series are obtained by filtering 1916–2010 data, which causes a 4-yr data loss at each end of the time series.

eastern Siberia are not associated with the SRP (cf. Figs. 2a,b). This discrepancy was also noticed by Wang et al. (2017), but the reason remains elusive. In addition, Wang et al. (2017) found that the SRP was not significantly affected by the Pacific decadal oscillation (PDO), but that negative (positive) SRP was more likely during positive (negative) AMO.

In this study we take a different approach to Wang et al. (2017): instead of separating the IA and ID components of the SRP, we seek to identify one mechanism for SRP variability on synoptic to decadal scales. We test the hypothesis that coherent precipitation variability in the Indian monsoon region is a common controlling mechanism for SRP variability. Hence, we start with the premise that ID and IA variability of the SRP can be understood as the low-frequency rectification of variability on shorter

scales. Implicitly, we consider that temperature anomalies associated with only the ID SRP (i.e. those in areas of Siberia and also North America and Greenland; cf. Figs. 2a–c) are not related to the SRP but are driven by another mechanism. We seek to clarify whether Atlantic and Pacific SST anomalies may cause SRP variability through their effect on the ISM. Our main goal is to explain the increase in ID SRP variability around the mid-1970s. To do so, we analyze two historical atmosphere-only climate simulations and four coupled climate simulations. The effects of SST forcing in the Atlantic and Pacific are further isolated in atmosphere-only simulations with prescribed phases of the AMO, and ocean–atmosphere coupled experiments with prescribed phases of decadal SST variability in the North Pacific and North Atlantic. We propose a mechanism

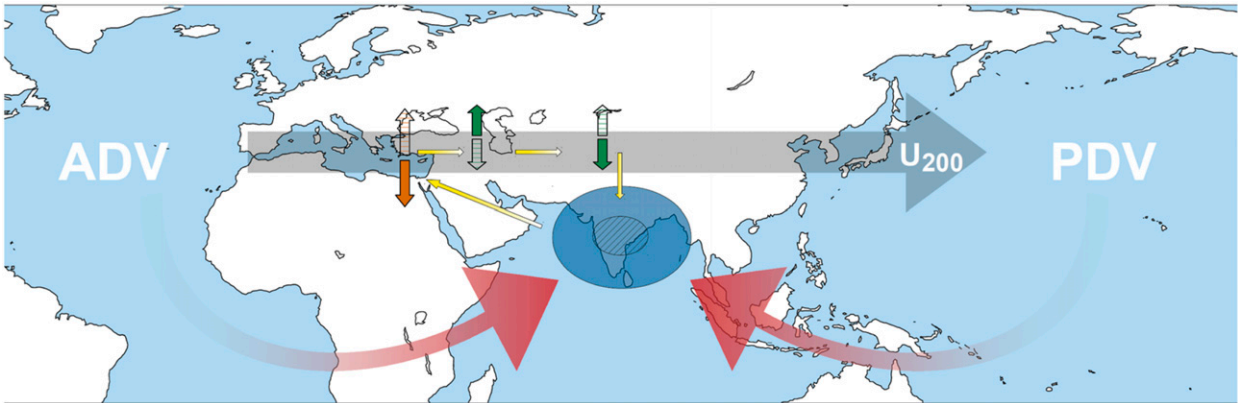


FIG. 4. Negative phases of Atlantic decadal variability (ADV) or Pacific decadal variability (PDV) lead to more coherent, stronger South Asian monsoon precipitation (red arrows and large blue ellipse). This leads to anomalous sinking motion over the Mediterranean region (orange arrow) through the monsoon–desert mechanism. A positive phase of the SRP is then induced downstream along the subtropical westerly jet (green arrows; first giving anomalous northward, then southward winds). The positive phase of the SRP induces anomalous rising motion over South Asia, reinforcing the monsoon in a positive feedback loop (yellow arrows). Positive phases of the ADV or PDV drive negative and less coherent rainfall anomalies over South Asia (small blue hatched ellipse). This leads to anomalous ascending motion over the Mediterranean (hatched orange arrow) and ultimately leads to anomalous sinking motion over South Asia, reinforcing the original anomaly.

for the recently increased SRP variability, which is summarized in Fig. 4: ocean variability on decadal time scales is associated with more coherent South Asian monsoon precipitation in recent decades. Through the monsoon–desert mechanism, this increased coherence in precipitation forces larger SRP amplitudes. To our knowledge, no previous study has addressed SRP variability in this way using observations and a hierarchy of targeted experiments.

Section 2 introduces the observational data, model simulations, and analysis methods. Results from numerical simulations are discussed in section 3. Observed IA and ID SRP variability is analyzed in section 4, and intraseasonal variability in section 5. Section 6 is a discussion and section 7 summarizes the main findings. For frequently used abbreviations, please see the definitions in Tables 1–4.

2. Data and methods

a. Observational data

For simplicity, we refer to reanalysis data as observations throughout the text. The reliability of the datasets is discussed in section 6.

Monthly-mean 1979–2016 200-hPa meridional winds V_{200} from the $0.7^\circ \times 0.7^\circ$ European Centre for Medium-Range Weather Forecasts (ECMWF) interim reanalysis (ERA-Interim; Dee et al. 2011) are used to study the recent ID variability of the SRP; for consistency with Wang et al. (2017) 1979–2010 data are used to define the SRP spatial pattern.

A longer record of the SRP is constructed based on 1900–2010 V_{200} from the $2.5^\circ \times 2.5^\circ$ ECMWF Twentieth Century

Reanalysis (ERA-20C; Poli et al. 2016). ERA-20C assimilates observations of surface pressure and marine winds only. The variability of the SRP in ERA-20C is almost identical to that in ERA-Interim over the common period, since 1979 (Wang et al. 2017). We also show maps derived from 1916–2010 500-hPa pressure velocity from ERA-20C.

For consistency with Wang et al. (2017), we use 1916–2010 JJA precipitation and 1.5-m air temperature from the $0.5^\circ \times 0.5^\circ$ University of Delaware monthly dataset

TABLE 1. Table of frequently used abbreviations.

Abbreviation	Expansion
SRP	Silk Road pattern
CGT	Circumglobal teleconnection
AMO	Atlantic multidecadal oscillation
PDO	Pacific decadal oscillation
ENSO	El Niño–Southern Oscillation
ISM	Indian summer monsoon
IA	Interannual
ID	Interdecadal
CEN	Causal effect network
MetUM	Met Office Unified Model
GOML	Global Ocean Mixed Layer coupled configuration of the MetUM
ATL	Atlantic
PAC	Pacific
GFDL	Geophysical Fluid Dynamics Laboratory
CAM	Community Atmosphere Model
CCM	Community Climate Model
CLIVAR	Climate Variability and Predictability, here: the set of GFDL, CAM, and CCM simulations

TABLE 2. Definitions of all CEN actors. From left, columns show the abbreviations used in the text; the geographical locations; the variables, where V_{200} stands for 200-hPa meridional wind, T for 2-m temperature, and ω for 500-hPa pressure velocity; and the latitude and longitude bounds for averaging, or the location of the grid point, respectively. All actors use pentad-averaged ERA-20C data for JJA from 1900 to 2010.

	Approx. location	Variable	Lat–lon bounds
SRP	SRP EOF region	SRP index	20°–60°N, 30°–130°E
V1	SRP peak 1	V_{200}	57°N, 17°E
V2	SRP peak 2	V_{200}	45°N, 47°E
V3	SRP peak 3	V_{200}	41°N, 79°E
V4	SRP peak 4	V_{200}	43°N, 111°E
V5	SRP peak 5	V_{200}	45°N, 145°E
NERU	Northeast Russia	T	60°–70°N, 140°–160°E
ARPI	Arabian Peninsula	T	25°–35°N, 40°–50°E
CEAS	Central Asia	T	35°–45°N, 60°–80°E
MONG	Mongolia	T	40°–50°N, 90°–110°E
WEUR	Western Europe	T	40°–50°N, 10°W–10°E
EEUR	Eastern Europe	T	45°–55°N, 30°–50°E
MED	Mediterranean	ω	30°–41°N, 17°–31°E
IND	Western India	ω	15°–28°N, 70°–80°E

(UDEL, version 4.01; Willmott and Matsuura 2001) in the analysis of IA and ID variability. This gridded dataset is based on station measurements and rain gauge data.

Monthly mean 1979–2010 SSTs are obtained from the $1^\circ \times 1^\circ$ Hadley Centre Sea Ice and SST dataset (HadISST; Rayner et al. 2003). The 1920–2006 AMO and PDO index are also based on HadISST, with global

warming trends removed; these are obtained from <http://climexp.knmi.nl>.

To analyze the SRP and its associated synoptic-scale variability, we use daily 1900–2010 V_{200} , 500-hPa vertical pressure velocity ω , and 2-m temperature T from ERA-20C.

b. Definition of the SRP

To directly compare to Wang et al. (2017), our definitions of the SRP index and its IA and ID components follow theirs.

The SRP is defined as the first empirical orthogonal function (EOF) of JJA-mean 1979–2010 ERA-Interim V_{200} in the “SRP domain” (20°–60°N, 30°–130°E), that is, a domain containing the Northern Hemisphere subtropical westerly jet stream over Eurasia. The corresponding normalized principal component (PC) time series is defined as the SRP index. For ERA-20C and our simulations (described in section 2d), the SRP index is the so-called pseudo-PC, defined as the projection of the dataset onto the 1979–2010 ERA-Interim spatial pattern within the SRP domain. Wang et al. (2017) showed that their results were insensitive to choosing slightly different domains or time periods for the EOF analysis.

To extract ID components from any given dataset, we use a 9-yr Lanczos low-pass filter (Duchon 1979). The IA component is the unfiltered time series minus the ID time series.

TABLE 3. For all simulations, columns show the abbreviations used in the text, atmospheric horizontal resolution, resolution at the equator, integration length (of each ensemble member), number of ensemble members, and details of the experiment. Please refer to the text for a description of the different configurations and experiments.

Simulation	Model	Resolution	Resolution at equator (km)	Length (yr)	No. of members	Configuration
A96	MetUM GA6	N96	208	27 (1982–2008)	1	AMIP
A216	MetUM GA6	N216	88	27 (1982–2008)	1	AMIP
C96	MetUM GC2	N96	208	100	1	Fully coupled
C216	MetUM GC2	N216	88	100	1	Fully coupled
C512a	MetUM GC2	N512	39	100	1	Fully coupled
C512b	MetUM GC2	N512	39	100	1	Fully coupled
PAC.C	MetUM GOML	N96	208	30	3	MC-KPP, cold Pacific
PAC.N	MetUM GOML	N96	208	30	3	MC-KPP, neutral Pacific
PAC.W	MetUM GOML	N96	208	30	3	MC-KPP, warm Pacific
ATL.C	MetUM GOML	N96	208	30	3	MC-KPP, cold Atlantic
ATL.N	MetUM GOML	N96	208	30	3	MC-KPP, neutral Atlantic
ATL.W	MetUM GOML	N96	208	30	3	MC-KPP, warm Atlantic
GFDL.C	GFDL AM2.1	$2^\circ \times 2.5^\circ$	280	50	1	SST-driven, cold AMO
CAM.C	NCAR CAM3.5	T85	155	50	1	SST-driven, cold AMO
CCM.C	LDEO/NCAR CCM3	T42	310	50	1	SST-driven, cold AMO
GFDL.W	GFDL AM2.1	$2^\circ \times 2.5^\circ$	280	50	1	SST-driven, warm AMO
CAM.W	NCAR CAM3.5	T85	155	50	1	SST-driven, warm AMO
CCM.W	LDEO/NCAR CCM3	T42	310	50	1	SST-driven, warm AMO
GFDL.N	GFDL AM2.1	$2^\circ \times 2.5^\circ$	280	50	1	SST-driven, neutral AMO
CAM.N	NCAR CAM3.5	T85	155	50	1	SST-driven, neutral AMO
CCM.N	LDEO/NCAR CCM3	T42	310	50	1	SST-driven, neutral AMO

TABLE 4. Linear correlation coefficients of the interannual JJA SRP index from ERA-20C (SRP), UDEL rainfall in northwest India (20° – 30° N, 70° – 80° E; P_{NIND}), southwest India (10° – 20° N, 70° – 80° E; P_{SIND}), to the north of the Bay of Bengal (15° – 28° N, 82° – 100° E; P_{NBEN}), and ERA-20C pressure velocity over the eastern Mediterranean Sea (30° – 41° N, 17° – 31° E) for the periods 1904–2006, 1904–70 and 1971–2006. Boldface numbers indicate that correlations are significant at the 90% confidence level.

	1904–2006	1904–70	1971–2006
SRP, P_{NIND}	0.33	0.31	0.34
SRP, P_{SIND}	0.16	0.09	0.25
P_{NIND} , P_{SIND}	0.59	0.48	0.75
SRP, P_{NBEN}	0.01	–0.03	0.09
P_{NIND} , P_{NBEN}	0.09	–0.17	0.41
SRP, ω_{MED}	0.45	0.36	0.59
P_{NIND} , ω_{MED}	0.40	0.38	0.42

Note that, by definition, the EOF algorithm requires removing the time mean from each grid point. When computing the SRP index for a dataset, we remove the time mean based on the entire length of the data. For comparing our experiments, however, this method would not allow us to detect offsets in the SRP index between one simulation and another. Therefore, we first form synthetic time series by concatenating V_{200} data from each simulation involved in the comparison. We then remove the time mean from the synthetic dataset and compute the pseudo-PC as usual.

To analyze intraseasonal SRP variability, we compute daily and pentad-mean pseudo-PC time series. Computing the daily SRP index combines all JJA days of a given set of years, before removing the mean of the entire time series. The computation of the pentad SRP index follows the causal effect network algorithm described below.

c. CEN analysis

To better understand how positive or negative SRP years arise from its intraseasonal evolution, we perform a causal effect network (CEN) analysis, following Kretschmer et al. (2016). Similar causal discovery analysis has been applied to various problems in atmospheric and oceanic science, such as the role of the North Atlantic overturning in global-mean temperature variability (Schleussner et al. 2014), Arctic drivers of the midlatitude winter circulation (Kretschmer et al. 2016), and tropical air–sea coupled processes (Runge et al. 2014, 2015).

We first select a set of variables that represent processes relevant to SRP variability. The SRP has five prominent V_{200} extrema over Eurasia (Fig. 1a,c), two of which are outside the SRP domain (golden box in Fig. 1c). We refer to V_{200} at these five locations as V1, V2, V3, V4

and V5, respectively, from west to east (magenta triangles in Fig. 1c). Regions with strong temperature anomalies identified in Figs. 2a and 2b are marked by green boxes in Fig. 1c. The SRP is correlated with precipitation over northwest India (Wang et al. 2017). To measure this influence, we diagnose the monsoon–desert mechanism, involving opposite-signed vertical motions over western India (IND) and the eastern Mediterranean (MED). IND and MED are marked by red boxes in Fig. 1c; their bounds are chosen to coincide with key locations defined in Tyrlis et al. (2013). Table 2 lists all variables and their locations.

One can expect that on scales from days to weeks most of the above variables are strongly autocorrelated and mutually correlated. However, we do not expect causal relationships between most of them. CEN allows us to separate cause and effect on intraseasonal time scales despite autocorrelations and common causes. We form pentad-mean time series of the variables in Table 2 and follow the steps described in Kretschmer et al. (2016), summarized below.

We compute a single time series for each variable, also called “actors” X , in Table 2 by computing area averages of T and ω in the boxes specified. For V_{200} we average over the $2^{\circ} \times 2^{\circ}$ area around the given coordinate. Anomaly time series are formed by removing the linear trend and climatological mean from each pentad, then combining the 30 JJA pentads of all years.

A set of causal “parents” $P_i \subset X$ is found for each actor $x_i \in X$ by performing iterative conditional independence tests using partial correlations. Note that P_i only consists of processes that are significantly correlated with x_i after removing the possible influence of all $x_j \in X$, including x_i itself, at lead times $\tau \in 1, \dots, 18$; that is, we test all lead times up to 90 days.

To quantify the strength of the causal relationship, all parents P_i are included in a multiple linear regression analysis. For each x_i we perform a set of multiple regressions: each multiple regression includes the parents P_i and one $x_k^{\tau} \in X$. The $x_k^{\tau} \in X$ include all actors in X at all lead times $\tau \in 0, \dots, 18$, except those that are already included in P_i . This second step allows us to determine the strength of causal links. These are defined as the partial regression coefficients β . This second step allows us to test, in a mathematically strict way, if β is significant at the 1% level.

d. Simulations

The observational record from 1920 onward indicates that the SRP is negatively correlated with the AMO and positively with the PDO (Fig. 2d). The IA (ID) correlation coefficients for 1920–2010 are -0.10 (-0.24) (AMO) and 0.10 (0.26) (PDO), but none of them is

statistically significant at the 90% confidence level (Wang et al. 2017). Based on observations alone, however, it is difficult to infer whether these correlations have a physical foundation or are due to chance. Our record of reliable observations is short relative to the period of slow modes of climate variability, such as the AMO and PDO. Furthermore, the AMO and PDO may not be independent. There is additional variability forced by other phenomena, such as ENSO (see section 1).

To help mitigate these difficulties and untangle possible causes of decadal-scale changes in the SRP, we analyze numerical simulations with models of varying complexity (Table 3). These include six climate simulations of the Met Office Unified model (MetUM): two historical AMIP-style simulations (A96, A216) of the Global Atmosphere 6.0 configuration (GA6; Walters et al. 2017) and four coupled simulations (C96, C216, C512a, and C512b) of the Global Coupled configuration 2.0 (GC2; Williams et al. 2015). The nodal number following “A” or “C” denotes the atmospheric horizontal resolution (see Table 3). The AMIP experiments test the impact (if any) of observed SST variability on the SRP in the recent period of 1982–2008. The GC2 experiments test the impact of simulated SST internal variability (if any) on the SRP over a much longer period, albeit with complicating effects of biases in mean SST and possible misrepresentations of modes of variability. We include experiments at different horizontal resolutions to increase the number of ensemble members. These experiments were previously analyzed by Stephan et al. (2018b), where more details of the simulations are given. Stephan et al. (2018a) showed that these simulations well capture extratropical Rossby wave propagation over Eurasia.

To isolate the impact of the AMO on the phase of the SRP in atmosphere-only global climate model simulations, we analyze simulations from the U.S. Climate Variability and Predictability (CLIVAR) Drought Working Group. The North Atlantic SST anomaly is calculated as the third rotated EOF of annual-mean 1901–2004 SSTs (Fig. 5e). The annual-mean anomaly is prescribed on top of a seasonally varying SST climatology. The U.S. CLIVAR experiments are available online at http://gmao.gsfc.nasa.gov/research/clivar_drought_wg/index.html and are described in Schubert et al. (2009). We analyze simulations from the Geophysical Fluid Dynamics Laboratory (GFDL) Atmosphere Model, version 2.1 (AM2.1; Delworth et al. 2006), the National Center for Atmospheric Research (NCAR) Community Climate Model, version 3.0 (CCM3.0; Kiehl et al. 1998), and the NCAR

Community Atmosphere Model, version 3.5 (CAM3.5; Neale et al. 2008).

Furthermore, we examine several integrations of the Global Ocean Mixed Layer coupled configuration of the MetUM (MetUM GOML2; Hiron et al. 2015), which couples GA6 to the multicolumn *K* profile parameterization ocean model (MC-KPP). Each one-dimensional ocean column is coupled to one atmospheric grid cell to allow the exchange of heat, moisture, and momentum every 3 h. The individual ocean columns simulate vertical mixing, but not advection. To account for the lack of advection and for biases in atmospheric surface fluxes, seasonally varying temperature and salinity tendencies are applied to the full MC-KPP column at each grid point. These tendencies constrain MC-KPP to a desired seasonally varying ocean mean state. Tendencies are computed from initial 10-yr GOML simulations, in which the MC-KPP is relaxed to the desired ocean mean state with a 15-day time scale. The mean seasonal cycle of tendencies from these simulations is then imposed in the simulations described below. This method ensures that the tendencies do not damp variability. See Hiron et al. (2015) for further details. The MC-KPP columns are 1000 m deep, with 100 points on a stretched grid for finer resolution near the surface; the top layer is 1.2 m thick.

To test the effect of SST variability in the Atlantic on the SRP, we constrain the ocean in GOML2 “ATL” experiments to a warm (ATL.W), cold (ATL.C), and neutral (ATL.N) background (Fig. 5a). The ATL SST anomaly is derived from the years 1925–61 (ATL.W) and 1962–96 (ATL.C), corresponding to a positive and a negative phase of the AMO, respectively. ATL.N is constrained to the 1925–96 average. Similarly, our GOML2 Pacific (“PAC”) experiments use warm (1976–2005; PAC.W), cold (1946–75; PAC.C), and neutral (1946–2005; PAC.N) SST backgrounds in the Pacific; the time period 1976–2005 (1946–75) corresponds to a positive (negative) phase of the PDO (Fig. 5b).

The target ocean mean states are constructed from the Met Office EN4 ocean analysis (version 4.2.0; Good et al. 2013). For the warm and cold experiments, annual-mean ocean temperature and salinity anomalies are computed relative to the neutral experiment, using the time periods specified above. These anomalies are then scaled by a factor of 3 (for the Atlantic) and 2 (for the Pacific) to give SST anomalies of similar magnitudes to those used in the CLIVAR AMO and PDO experiments. The anomalies are imposed on the mean seasonal cycle of the neutral experiment, only in the basin of interest, and only north of 20°S. A five-grid-point transition region at the 20°S boundary

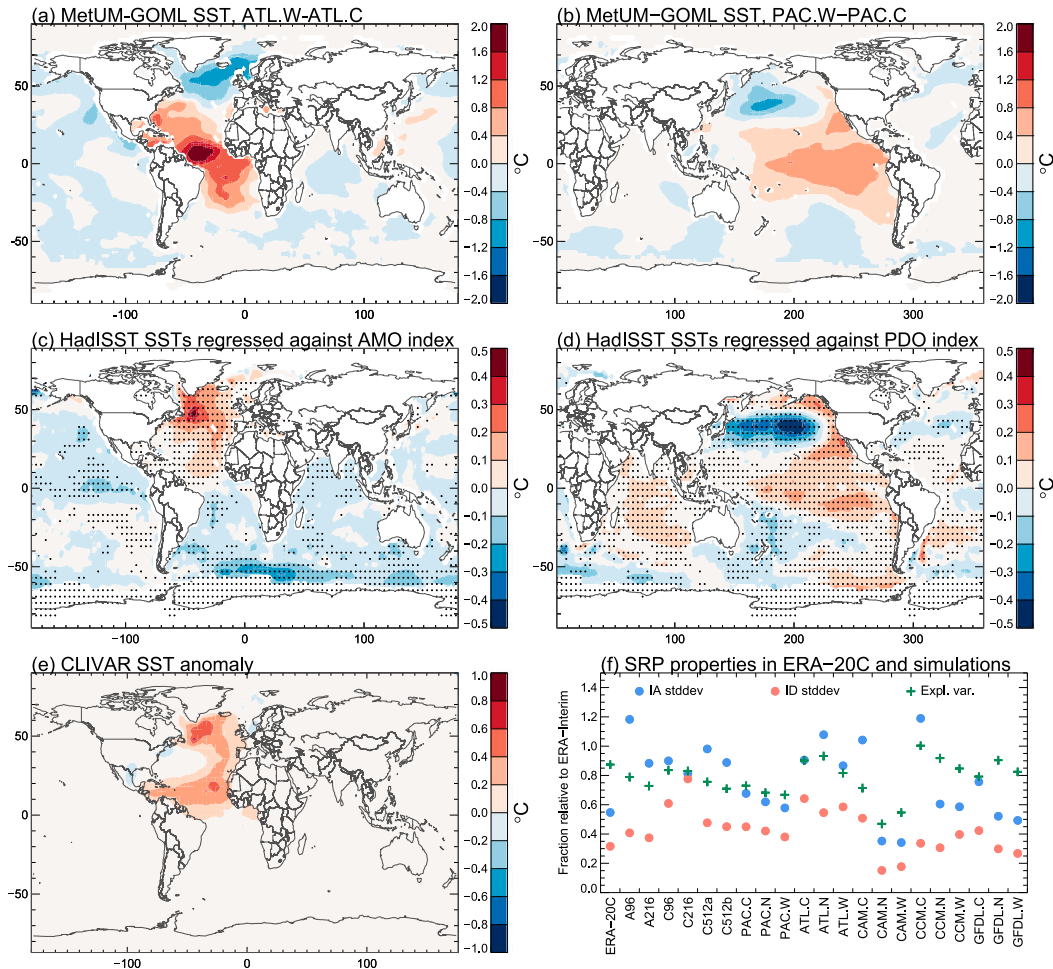


FIG. 5. Composites of simulated SST anomalies from the GOML (a) ATL and (b) PAC experiments, and regression of 1920–2006 detrended and filtered HadISST SSTs against the normalized ID component of the (c) AMO and (d) PDO indices. (e) The SST anomaly used in the CLIVAR AMO experiments. (f) For the JJA SRP index in ERA-20C (1904–2006) and each simulation (full length), the fraction of IA and ID standard deviation (circles) relative to ERA-Interim (1979–2016). Also shown (plus symbols) is the fraction of the SRP-explained variance in V_{200} in the SRP domain (20° – 60° N, 30° – 130° E) relative to that in ERA-Interim. For the GOML PAC and GOML ATL experiments, the values shown correspond to the ensemble average.

blends the anomalies and the climatology. We emphasize that the GOML experiments are constrained not to idealized AMO or PDO phases, but to ocean temperature and salinity anomalies extracted from multidecadal periods of interest. While these periods correspond to AMO and PDO phases, the imposed ocean anomalies also contain the influence of other phenomena.

3. SRP variability in simulations and reanalysis

Figure 5f compares the variability of the SRP in 1900–2010 ERA-20C and all simulations to that in 1979–2016 ERA-Interim. ID variability in the longer ERA-20C period is only a third of that in ERA-Interim, highlighting

again that ID variability has increased since the mid-1970s in reanalysis data (Fig. 1b). IA and ID variability in all MetUM and CLIVAR simulations varies from close to ERA-20C to about 20% greater than ERA-Interim, indicating that the simulations produce a degree of variability that is consistent with observations. SRP variance does not systematically change with resolution or air–sea coupling in MetUM. Figure 5f also shows the SRP-explained fraction of V_{200} variance inside the SRP domain relative to ERA-Interim. Values are between ~ 0.7 and 1.0 except for CAM.N and CAM.W, where they are ~ 0.5 – 0.6 , but these simulations also have the smallest variability. Overall, the simulations capture the SRP, consistent with Kosaka et al. (2009).

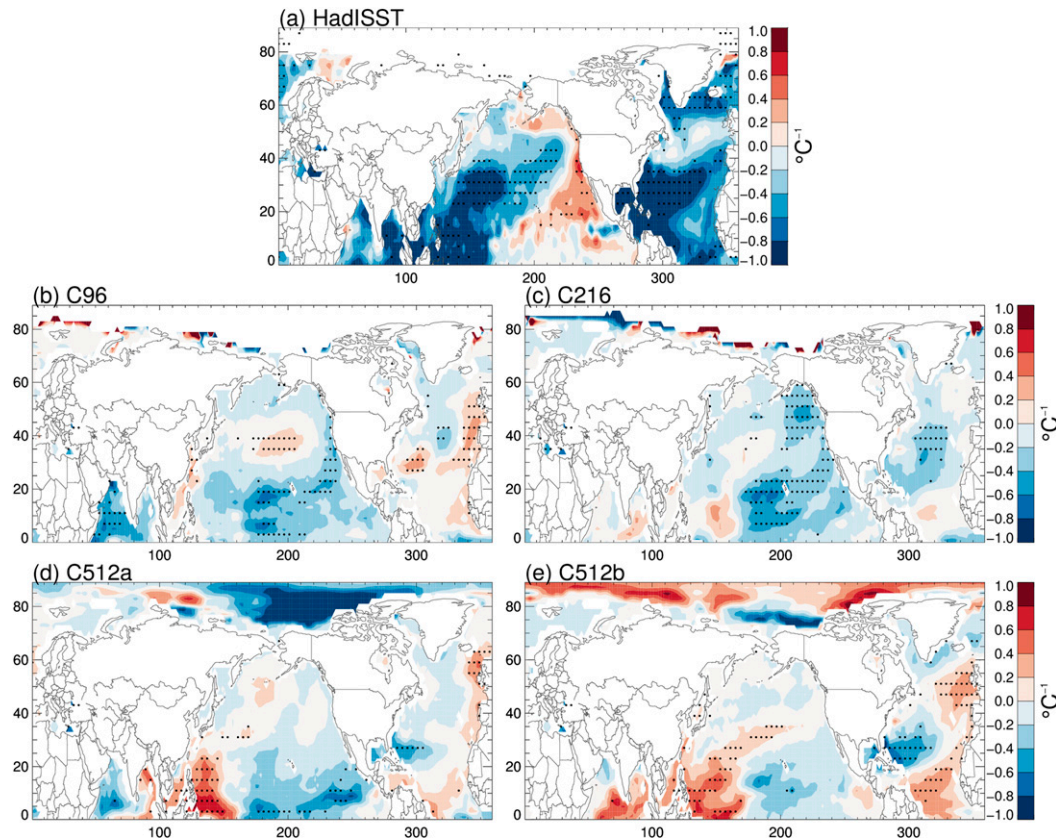


FIG. 6. Regression of (a) the normalized 1979–2010 ERA-Interim SRP index against observed 1979–2010 JJA SSTs, and (b)–(e) the normalized SRP indices for each MetUM GC2 simulation against simulated JJA SSTs. Stippling indicates significance at the 10% level.

We next examine the relationship between SRP variability and SSTs in observations and MetUM GA6 and GC2. As noted by Wang et al. (2017), a positive unfiltered 1979–2010 ERA-Interim SRP index is associated with SST anomalies that resemble a negative AMO and a positive PDO (Figs. 6a and 5c,d). The 1982–2007 A96 and A216 simulations use observed SSTs and historical solar, aerosol, and greenhouse gas forcings. Neither A96 nor A216 produces the observed SRP variability. Correlations of their SRP indices with that of ERA-Interim are only 0.26 (A96) and 0.14 (A216). The four GC2 simulations do not show consistent SST anomalies associated with the SRP, either with each other or with observations (Figs. 6b–e). Thus, the SRP in GC2 is not linked to realistic coupled modes of decadal variability.

Starting with the CLIVAR AMO experiments, we next analyze targeted simulations from reduced-complexity models. We compute the SRP index from synthetic time series that combine the warm, cold, and control simulations of each model (GFDL, CAM, CCM), as outlined in section 2b. The average normalized

SRP indices in GFDL are +0.03, -0.14 , and +0.04 for the cold, neutral, and warm AMO simulations, respectively; -0.05 , +0.14, and -0.09 in CAM; and 0.04, -0.16 , and 0.12 in CCM. Therefore, the imposed AMO SST anomaly does not systematically modulate the SRP. This is consistent with MetUM A96 and A216.

The above findings support the hypothesis of Kosaka et al. (2012) that the ocean does not force the SRP, which they suggested explained why models showed low seasonal prediction skill for the SRP phase. Nevertheless, we cannot conclude that SST variability is irrelevant to SRP variability, as the SST signal may be mediated through the ISM (Krishnan and Sugi 2003; Goswami et al. 2006; Joshi and Rai 2015). The GA6 and GC2 simulations may not correctly capture these teleconnections. We discuss this further in section 6.

The GOML experiments include air–sea coupling with minimal SST biases relative to the desired mean ocean state. The ATL and PAC GOML experiments consist of three 30-yr simulations each for the warm, cold, and control ocean states in the respective basins

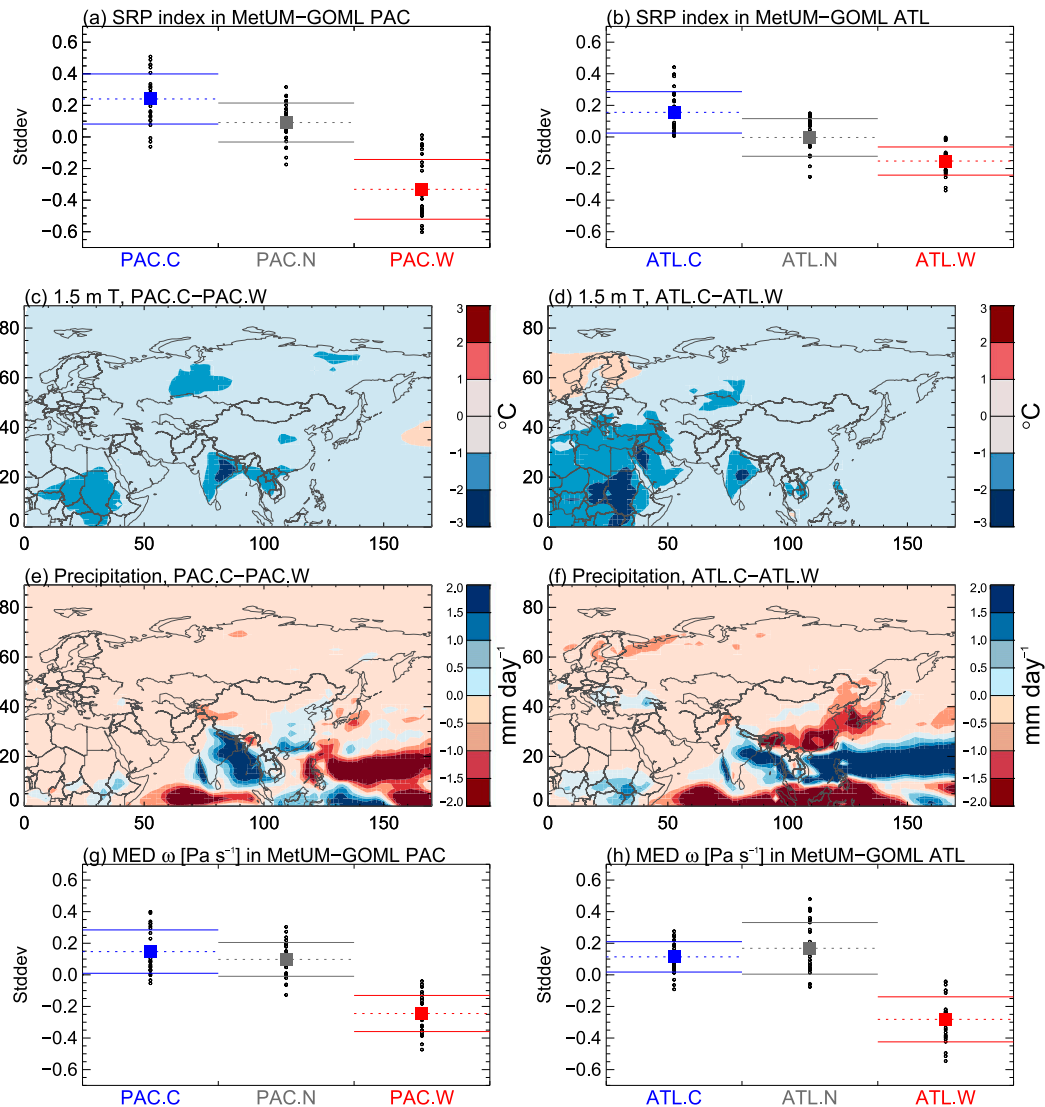


FIG. 7. Results from GOML experiments: (a) the average phase of the SRP index for the 27 synthetic time series constructed from the PAC experiments (dots), with their mean (box) and standard deviation (solid horizontal lines). Also shown are composites of (c) 1.5-m temperature and (e) precipitation for PAC.C–PAC.W. (g) As in (a), but for 500-hPa pressure velocity over the eastern Mediterranean Sea (30° – 41° N, 17° – 31° E). (b), (d), (f), (h) As in (a), (c), (e), and (g) respectively, but for the GOML ATL experiments. For each SST experiment (PAC and ATL), the 27 synthetic time series are constructed by combining cold, neutral, and warm ensembles (three members each) in every possible way, using one cold, one neutral, and one warm run.

(Table 3). This allows us to compute 27 synthetic time series for each set of experiments (PAC and ATL). The average SRP phases of these 27 time series are shown in Figs. 7a and 7b. For both PAC and ATL, the phase of ocean variability shifts the SRP phase significantly. Composites of temperature (Figs. 7c,d) and precipitation (Figs. 7e,f) show that both cold simulations (PAC.C and ATL.C) have common anomalous wet conditions over India relative to the warm simulations (PAC.W and ATL.W); this is consistent with observed decadal ISM variability associated with Atlantic and Pacific forcing

(Krishnan and Sugi 2003; Goswami et al. 2006; Joshi and Rai 2015).

Precipitation in India is correlated with the SRP index in observations and in GA6 and GC2 (not shown). This makes it difficult to infer whether precipitation anomalies over India occur in response to an anomalous SRP or drive an anomalous SRP (Ding and Wang 2005, 2007). The GOML simulations, on the other hand, suggest that precipitation anomalies over India may be responsible for modulating the SRP phase via their impact on the west-central Asian high,

connected to the monsoon–desert mechanism (Tyrlis et al. 2013). To provide evidence for this mechanism in GOML, in Figs. 7g and 7h, we reproduce Figs. 7a and 7b, but this time for pressure velocity over MED (see Table 2 for definition). Subsidence over MED is indeed increased or decreased by about the same order of magnitude as the SRP index in Figs. 7a and 7b.

The nonlinearity in Fig. 7h occurs because SST anomalies in the ATL GOML simulations do not only induce precipitation anomalies over India, but also a meridional dipole pattern over Europe with drier (wetter) conditions over northern (southern) Europe in ATL.C and vice versa in ATL.W. Thus in ATL.C and ATL.W, precipitation anomalies over southern Europe and India are of the same sign; rising (sinking) over southern Europe compensates the sinking (rising) induced by rising (sinking) over India. In ATL.N there is no dipole anomaly over Europe but ATL.N still shows wet anomalies along the southern Himalayas. It is likely that this induces sinking over the Mediterranean, which in ATL.N is not compensated, explaining why ATL.N has the most positive ω_{MED} in Fig. 7h. Recall, however, that while the monsoon–desert mechanism is connected with a modulation of the SRP, the vertical motion over MED is not the immediate cause for a weaker or stronger SRP. Hence, the SRP response in Fig. 7b is still linear.

4. Observed IA and ID SRP variability

Since the SRP index is based on EOF analysis, it is instructive to examine the temporal variability of the SRP's individual V_{200} peaks (magenta triangles in Fig. 1c). Time series of normalized 1979–2016 ERA-Interim V_{200} at these peaks are shown in Figs. 8b–f. Peaks V2–V4 exhibit the strongest decadal shift. If the decadal shift of the SRP had its source over Europe, we would expect V1 to show a pronounced decadal shift. Instead, Figs. 8a–f are consistent with an upstream impact of South Asia, which mainly affects V2–V4.

We now inspect the relationship between IA and ID SRP variability and precipitation over South Asia. Figure 8g shows time series of the SRP index and JJA precipitation over northwest India P_{NIND} and southwest India P_{SIND} . The synchronicity of P_{NIND} and P_{SIND} has increased since the mid-1970s: the correlation between P_{NIND} and P_{SIND} increased from 0.48 in 1904–70 to 0.75 in 1971–2006 (Table 4). The small correlation of 0.09 between the SRP and P_{SIND} before 1970 suggests that the SRP does not drive P_{SIND} variability (Table 4). Instead, recall that northwest and southwest India (NIND and SIND) and the area to the north of the Bay of

Bengal (NBEN) are important for driving the monsoon–desert mechanism (Tyrlis et al. 2013). In fact, Cherchi et al. (2014) showed that the strongest anomalous vertical motion over the Mediterranean (MED) region occurred when they forced their linear baroclinic model with combined heating over the Arabian Sea and the Bay of Bengal. The increase in synchronicity between P_{NIND} and P_{NBEN} is substantial as well (Table 4): P_{NIND} and P_{NBEN} were insignificantly negatively correlated (-0.17) before 1970 and positively correlated ($+0.41$) after. The ID variability of the SRP has increased since P_{NIND} , P_{SIND} , and P_{NBEN} became synchronized. In addition, the correlations between ω_{MED} and the SRP, and ω_{MED} and P_{NIND} became stronger.

5. Observed synoptic SRP variability

SRP variability involves Rossby wave propagation and monsoon precipitation, which have typical time scales of ~ 2 – 10 days. To better understand how positive or negative SRP years derive from these synoptic-time-scale processes, we now investigate the relationship between South Asia and the SRP on synoptic time scales.

Figure 9 examines the intraseasonal variability of the SRP for particularly positive and negative years based on the normalized daily 1900–2010 ERA-20C SRP index. The SRP has similar intraseasonal properties in positive and negative years (Fig. 9a). The autocorrelations (Fig. 9b) and power spectra (Fig. 9c) in positive and negative years are very similar, such that the distributions of daily SRP indices are merely shifted by the seasonal-mean anomaly (Fig. 9d). Thus, positive and negative years do not derive from a few extreme days or from different properties of the Rossby waves responsible for the SRP. Instead, there is a systematic reinforcement of background states that leads the Rossby wave signature along the Eurasian jet to project more preferably onto the positive or negative SRP phase, respectively.

To investigate how different processes modulate this background state on synoptic time scales, we applied CEN analysis to pentad time series of the ERA-20C variables listed in Table 2 and shown in Fig. 1c. Figures 10a–c show the effects of the variables listed on the x axes (called parents) on the variables listed on the y axes (called actors). Each colored box shows the partial correlation coefficient of a particular parent–actor pair after removing the influence of the other parents on the actor. The lead time at which this correlation is strongest is written inside each colored box. Thus, green boxes indicate that a parent variable is positively correlated with an actor variable, and pink

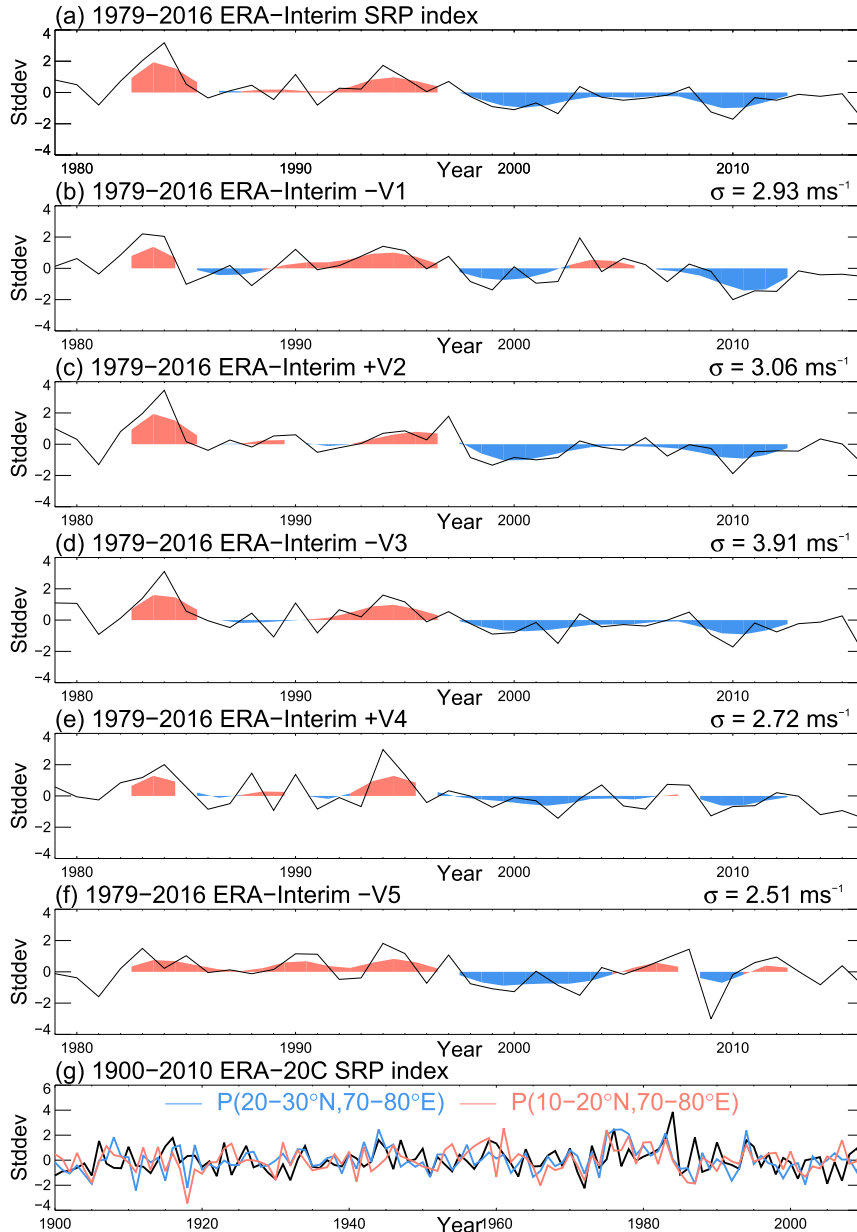


FIG. 8. ID variability of the SRP: JJA-mean time series (black lines) and their ID components (blue and red shading) for the (a) normalized 1979–2016 ERA-Interim SRP index and (b)–(f) normalized 1979–2016 ERA-Interim V_{200} at the peak locations of the SRP, as defined in Table 2 and shown in Fig. 1c. For V1, V3, and V5 the sign is flipped such that V1–V5 are positively correlated with the SRP index. The standard deviation σ of the original time series (black line) is shown above each panel. (g) The 1900–2010 ERA-20C SRP index (black) and normalized JJA UDEL rainfall time series in northwest India (blue) and southwest India (red).

boxes indicate negative correlations. Where parent and actor are identical, the colors indicate partial autocorrelations. The CEN analysis clearly captures the eastward propagation of the SRP (Fig. 10a). For example, V2–V4 lag V1; V3–V4 lag V2; V4–V5 lag V3; and V5

also lags V4. Wind extrema in the west lead wind extrema in the east; the signs of the correlations are such that positive and negative extrema alternate, as shown in Fig. 1a. Hence, the Rossby waves clearly originate over Europe.

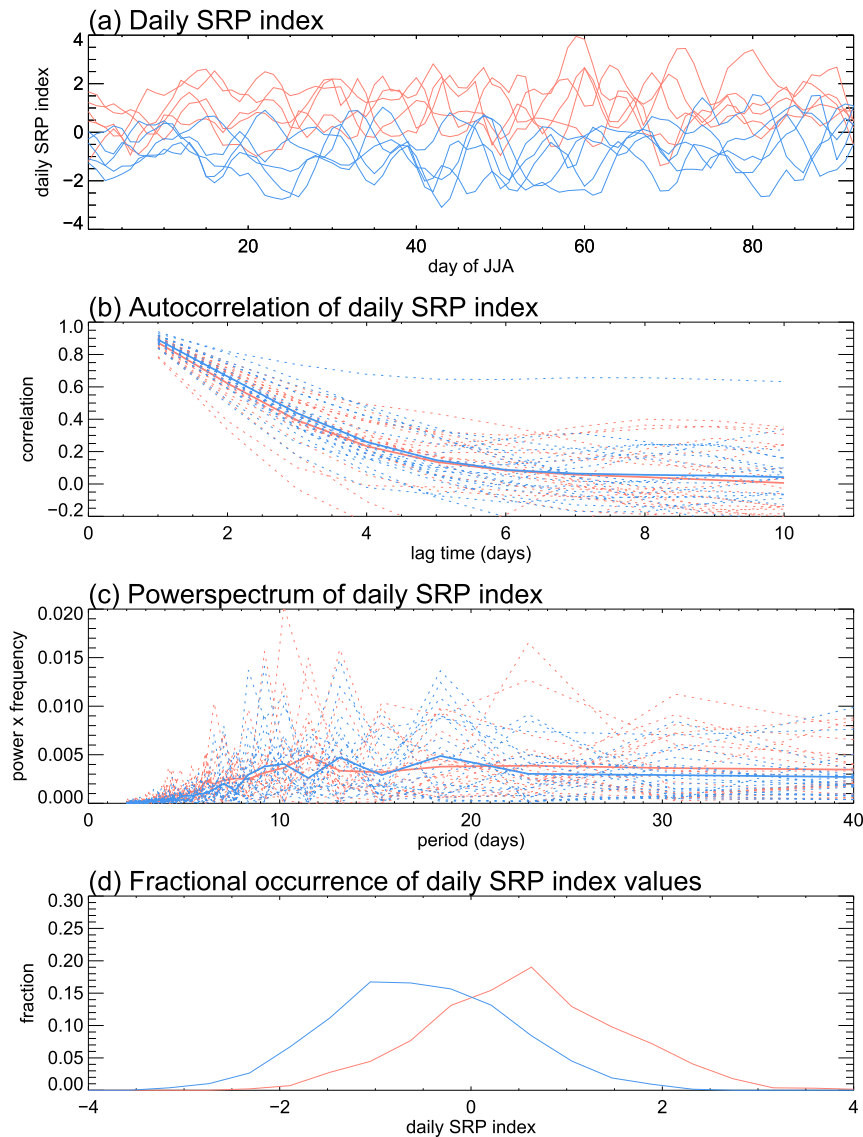


FIG. 9. Intraseasonal variability of the SRP. All panels use the normalized daily 1900–2010 ERA-20C SRP index in JJA: (a) SRP index for the five most positive (red) and negative (blue) years of the seasonal SRP index. (b) Autocorrelations for the 20 most positive (red) and negative (blue) years of the seasonal SRP index (dashed lines), and their averages (thick solid lines). (c) Power spectra for the 20 most positive (red) and negative (blue) years of the seasonal SRP index (dashed lines), and their average (thick solid lines). (d) Fractional occurrence of daily SRP index values for the 20 most positive (red) and negative (blue) years of the seasonal SRP index.

Figure 10b shows the effect that the SRP and V1–V5 have on 2-m temperature in different areas. Temperature in western and eastern Europe is affected by V1; temperature in Mongolia is affected by V2. Temperature in central Asia lags V1 and V2; temperature over the northern Arabian Peninsula lags V3. However, temperature over eastern Siberia is not affected by the SRP. This is consistent with the fact that the IA component of the SRP does not show significant

temperature anomalies over eastern Siberia. This supports our hypothesis that temperature anomalies in this region may not be driven by the SRP (Figs. 2a,b).

Finally, the CEN analysis confirms a positive feedback loop between vertical motion over IND and MED and the SRP (Fig. 10c). For example, in the positive SRP phase, V3 northerlies precede rising motion over IND. Rising motion over IND induces sinking over MED. Sinking over MED precedes V2 southerlies and V3

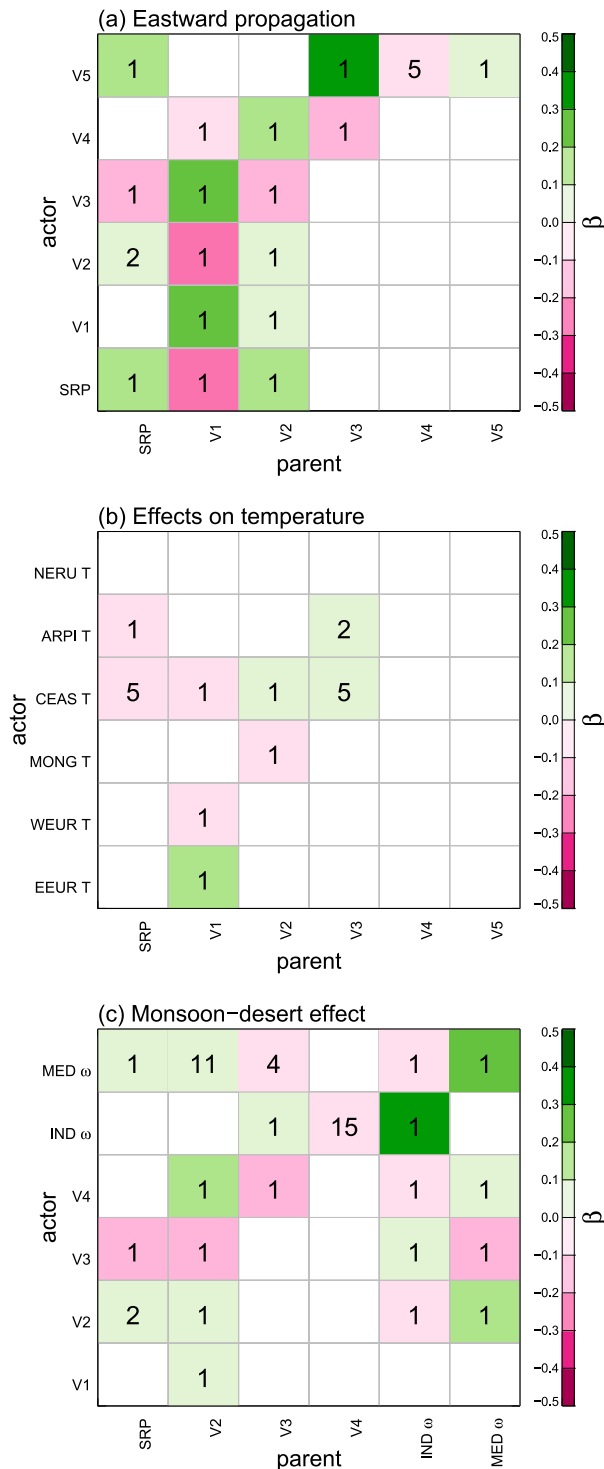


FIG. 10. Results from the intraseasonal CEN analysis based on ERA-20C: the partial-correlation coefficients β by selected parents (“cause”) and actors (“effect”), as defined in Table 2 and shown in Fig. 1c, showing (a) evidence of the eastward propagation of SRP anomalies, (b) the effects that the SRP and associated V_{200} anomalies have on temperature in specific locations, and (c) evidence that the monsoon-desert mechanism provides a positive feedback loop. All correlations shown are significant at the 1% level. Numbers indicate the lead time in units of pentads.

northerlies (i.e., the positive phase of the SRP). This feedback loop operates on synoptic time scales and can modulate the background state of the atmosphere to resemble the positive or negative phase of the SRP.

Summers with anomalous South Asian monsoon precipitation would trigger this feedback loop, explaining how coherent summer rainfall anomalies over SIND, NIND, and NBEN can create an anomalous SRP summer.

We chose the IND area for the CEN algorithm because it is important for driving the monsoon-desert mechanism (Tyrlis et al. 2013) and because the SRP is associated with strong precipitation anomalies there. We repeated the analysis with NBEN also included, but this did not change any of the above conclusions.

6. Discussion

If precipitation anomalies over South Asia are responsible for the ID SRP variability, as suggested by our analysis of GOML simulations and observations, then we should be able to explain why the observed relationships between SRP variability and SSTs are not found in GA6 and GC2 (A96, A216, C96, C216, C512a, C512b) or the CLIVAR AMO atmosphere-only experiments.

The magnitudes of the IA SRP variability in all six GA6 and GC2 simulations are closer to ERA-Interim (i.e., 1979–2016) than to ERA-20C (i.e., 1900–2010) (Fig. 5f). This is consistent with coherent IA rainfall variability over South Asia in these simulations; correlations between simulated P_{NIND} and P_{SIND} are between 0.40 (A96) and 0.69 (C512a), while those between P_{NIND} and P_{SIND} are between 0.21 (A216) and 0.64 (C216). These values are indeed closer to the post-1970 observed value (Table 4).

However, interannual simulated precipitation over India in A96 and A216 differs substantially from observations with correlations of -0.08 (A96) and -0.1 (A216) between simulated and observed precipitation averaged over northwest India (20° – 30° N, 70° – 80° E) for the common period. A96 and A216 do not reproduce the observed record of ISM precipitation despite observed SST forcing, which is a common problem in AMIP simulations (Kumar et al. 2005). Thus, these simulations do not correctly represent the phase relationships between observed SSTs and the ISM, and therefore do not reproduce the observed year-to-year SRP variability over 1982–2008.

The GC2 simulations do not correctly capture the teleconnections of ISM rainfall to slow modes of ocean variability in the North Atlantic, as expected from Goswami et al. (2006). The regression of simulated P_{NIND} against SSTs (Figs. 11a–d) reveals that P_{NIND} is

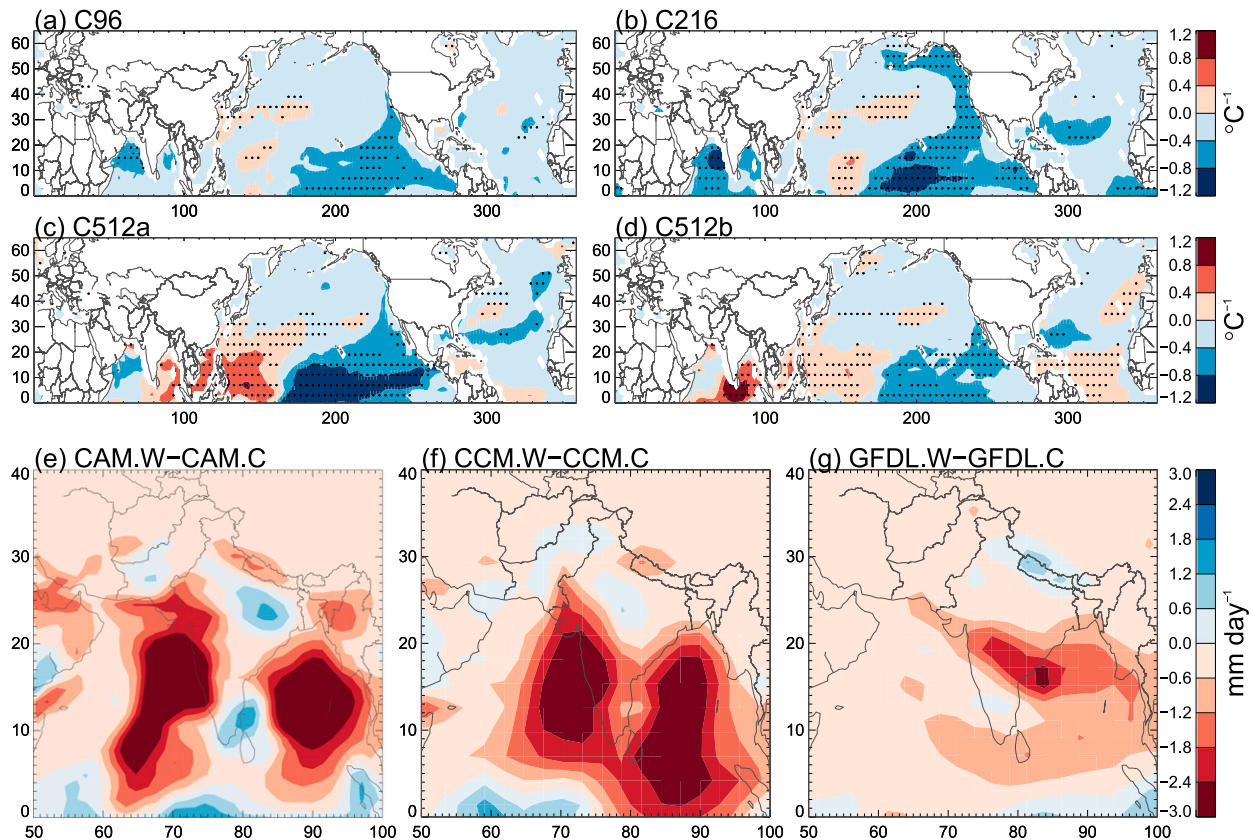


FIG. 11. (a)–(d) Regression of the normalized JJA P_{NIND} time series against SSTs in the GC2 simulations. Stippling indicates significance at the 10% level. (e)–(g) Composite precipitation anomalies from the CLIVAR experiments.

not driven by the AMO. On the other hand, the four GC2 simulations associate P_{NIND} with an SST pattern in the North Pacific that resembles the cold PDO phase, which is consistent with the wet conditions over NIND in the GOML PAC.C simulations.

The CLIVAR models show different patterns of anomalous precipitation over India in response to idealized AMO forcing with both wetter and drier areas (Figs. 11e–g). CAM produces dry anomalies in the mountainous terrain of northern India, the east coast and west coast, and in the area to the north of the Bay of Bengal, and wet anomalies in south and central India (warm minus cold phase); CCM produces dry anomalies along the Himalayas, wet anomalies in central India, and dry anomalies along the coasts and in southern India. GFDL produces wet (dry) anomalies in the northern (southern) half of India. This lack of coherent precipitation anomalies over India in each of these models likely explains why there are no consistent shifts of the SRP phase in response to the AMO, since the regional diabatic heating anomaly arising from the convective signal will not be large enough to excite perturbations in the wave response to the west.

Our results rely on reanalysis and rain gauge data. Both datasets may have errors that stem from the spatiotemporal incompleteness of the observational field, particularly in the early half of the twentieth century, variations in the density of observations and type of instruments, and errors in numerical algorithms (Thorne and Vose 2010). However, Wang et al. (2017) showed that the regime shifts of the ID SRP in 1972 and 1997 are consistent across five sets of reanalyses. Furthermore, they showed that these regime shifts and the increased ID variability after 1970 are still found when linear trends are removed.

To ensure that our conclusions based on JJA-seasonal average UDEL data are robust, we compared UDEL to the Asian Precipitation–Highly Resolved Observational Data Integration toward Evaluation of Water Resources (APHRODITE; Yatagai et al. 2012). APHRODITE has a high density of rain gauges over India; the high quality of the data for India has been confirmed (Rajeevan and Bhatte 2009; Krishnamurti et al. 2009). For the 20 years before and after 1970 the correlations between P_{NIND} and P_{SIND} in APHRODITE are 0.41 and 0.72, respectively. In UDEL they are 0.38 and 0.82, respectively. Thus there is clear enhanced spatial

coherency of rainfall in India following 1970. For the whole period (1950–90), the correlations between APHRODITE and UDEL are 0.90 for P_{NIND} and 0.89 for P_{SIND} , indicating strong consistency between the two datasets. Note that the increase in synchronicity of P_{NIND} and P_{SIND} around 1970 is also consistent with the increase in synchronicity of both the SRP and P_{NIND} with ω_{MED} in ERA-20C. ERA-20C may be considered independent of APHRODITE and UDEL because ERA-20C only assimilates surface pressure and marine wind observations.

While the PAC and ATL SST patterns in GOML have a specific effect on the SRP, which we argued is mediated through changes in precipitation over South Asia, we cannot be certain that these SST patterns would have the same effect in reality. Similarly, even though GC2 and GA6 did not produce a consistent relationship between SRP and SST variability, it may very well be that SSTs influence the SRP in reality through mechanisms that are not correctly captured by models. Such mechanisms could include, for instance, the effects of ENSO on the location of heat sources over South Asia (Ding and Wang 2005), or of the AMO and PDO on the ISM (Krishnan and Sugi 2003; Goswami et al. 2006; Joshi and Rai 2015). Zhang et al. (2008) found that the standard deviation of Niño-3 SST anomalies increased from $\sim 0.65^{\circ}\text{C}$ in the 1940s to $\sim 0.95^{\circ}\text{C}$ in recent decades. It is possible that the increase in ENSO and SRP amplitudes are related through ENSO modulation of South Asian precipitation. However, it is beyond the scope of this study to investigate the relationship between any particular pattern of SST variability and the SRP.

The meridional structure of the precipitation anomalies over the western Pacific produced by the GOML SST experiments (Figs. 7e,f) resembles precipitation anomalies associated with the Pacific–Japan pattern (Kosaka et al. 2013) and with the motion of the western Pacific subtropical high (Yang et al. 2017). Dynamically, these patterns are unlikely to influence the SRP because their associated circulation anomalies occur downstream of the SRP. We cannot exclude that the SRP could modulate the Pacific–Japan pattern. Alternatively, the SRP and downstream patterns could be modulated by ISM precipitation. Understanding the links between the SRP, the Pacific–Japan pattern, and precipitation variability that is associated with the western Pacific subtropical high is outside the scope of the paper.

Based on regressions of surface temperature against the SRP and AMO indices and results from the CEN analysis, we argued that it is plausible that temperature anomalies in the midlatitudes of Eurasia are driven by the AMO, but we did not investigate the mechanism. Wang et al. (2017) associated these midlatitude anomalies with an ID version

of the SRP that has a different spatial structure with a greater meridional extent than the IA SRP, while we treated the SRP as having a consistent spatial structure across all time scales. Both are valid approaches and we suggest interpreting the ID version of the SRP in Wang et al. (2017) and associated temperature anomalies in eastern Siberia as a different teleconnection pattern that may be forced by the AMO. Similarly, the northward extension of the ID SRP may be interpreted as a mixture of the traditional SRP and other signals. Our study examined the traditional SRP, but investigating the ID teleconnection and its potential link to the AMO could be an interesting avenue for future research.

7. Summary

Substantial surface air temperature and precipitation anomalies in Eurasia are associated with SRP variability (Lu et al. 2002; Wu 2002; Enomoto et al. 2003; Ding and Wang 2005; Huang et al. 2011; Chen and Huang 2012; Saeed et al. 2011, 2014; Hong and Lu 2016; Wang et al. 2017). Many factors have been proposed to modulate the SRP phase on interannual to interdecadal scales, including SSTs and/or convective anomalies in the Atlantic, Pacific, and Indian Oceans (Lu et al. 2002; Chen and Huang 2012; Ding et al. 2011; Ding and Wang 2005). Our findings suggest that the ocean does not directly force the SRP, as also argued by Kosaka et al. (2012). Understanding the physical mechanism responsible for the variability of the SRP is particularly important because contemporary initialized coupled prediction systems cannot reliably predict the phase of the SRP at monthly to seasonal lead times (Kosaka et al. 2012).

Our analysis of air–sea coupled and atmosphere-only climate simulations—the latter forced with observed SSTs, and with prescribed SST anomalies resembling the AMO—showed that none of these simulations associated SRP variability with a consistent SST pattern. Furthermore, we analyzed six GOML experiments, in which the atmosphere is coupled to one-dimensional ocean columns that allow easily constraint of the ocean mean state to a target climatology. These simulations, constrained to different phases of decadal variability in the Atlantic and Pacific separately, produced precipitation anomalies over South Asia, consistent with observational and modeling studies based on the PDO and AMO, that we argued were responsible for the significant shifts of the SRP phase between these GOML experiments. The SRP was in a more positive phase in those GOML experiments with wet conditions over South Asia, associated with cold phases of decadal variability in the tropical Atlantic and the Pacific.

Based on these results we investigated the possibility that convection associated with the South Asian summer monsoon is responsible for the decadal variability of the SRP. We applied causal effect network analysis to variables from ERA-20C that play a key role in the monsoon–desert mechanism (Rodwell and Hoskins 1996; Ding and Wang 2005; Ding et al. 2011; Tyrlis et al. 2013; Cherchi et al. 2014). This confirmed the existence of a positive feedback loop between the SRP and vertical motion over India and the Mediterranean (Fig. 4). Through this mechanism anomalous South Asian monsoon precipitation is able to reinforce the positive or negative phase of the SRP on intraseasonal time scales. By analyzing the properties of the SRP on synoptic time scales, we found that a positive or negative SRP year can be understood as the low-frequency rectification of variability on synoptic time scales. We showed that the intraseasonal variability of the SRP does not necessarily feed back onto the decadal SRP variability. Rather, the decadal variability alters the atmospheric background state on which intraseasonal SRP variability occurs. Importantly, JJA rainfall over northwest India, southwest India, and an area over and to the north of the Bay of Bengal have become more synchronized since the mid-1970s, consistent with stronger decadal variability in the monsoon since that time. These areas were shown to be most important for triggering the monsoon–desert mechanism (Tyrlis et al. 2013; Cherchi et al. 2014). Thus, we found a plausible explanation for the stronger interdecadal SRP variability than earlier in the twentieth century.

Acknowledgments. This work and its authors, C. C. Stephan and A. G. Turner, were supported by the UK–China Research and Innovation Partnership Fund through the Met Office Climate Science for Service Partnership (CSSP) China as part of the Newton Fund. Nicholas Klingaman was supported by an Independent Research Fellowship from the Natural Environment Research Council (NE/L010976/1).

REFERENCES

- Chen, G., and R. Huang, 2012: Excitation mechanisms of the teleconnection patterns affecting the July precipitation in northwest China. *J. Climate*, **25**, 7834–7851, <https://doi.org/10.1175/JCLI-D-11-00684.1>.
- , —, and L. Zhou, 2013: Baroclinic instability of the Silk Road Pattern induced by thermal damping. *J. Atmos. Sci.*, **70**, 2875–2893, <https://doi.org/10.1175/JAS-D-12-0326.1>.
- Cherchi, A., H. Annamalai, S. Masina, and A. Navarra, 2014: South Asian summer monsoon and the eastern Mediterranean climate: The monsoon–desert mechanism in CMIP5 simulations. *J. Climate*, **27**, 6877–6903, <https://doi.org/10.1175/JCLI-D-13-00530.1>.
- Dee, D. P., and Coauthors, 2011: The ERA-Interim reanalysis: Configuration and performance of the data assimilation system. *Quart. J. Roy. Meteor. Soc.*, **137**, 553–597, <https://doi.org/10.1002/qj.828>.
- Delworth, T. L., and Coauthors, 2006: GFDL’s CM2 global coupled climate models. Part 1: Formulation and simulation characteristics. *J. Climate*, **19**, 643–674, <https://doi.org/10.1175/JCLI3629.1>.
- Ding, Q.-H., and B. Wang, 2005: Circumglobal teleconnection in the Northern Hemisphere summer. *J. Climate*, **18**, 3483–3505, <https://doi.org/10.1175/JCLI3473.1>.
- , and —, 2007: Intraseasonal teleconnection between the summer Eurasian wave train and the Indian monsoon. *J. Climate*, **20**, 3751–3767, <https://doi.org/10.1175/JCLI4221.1>.
- , —, J. M. Wallace, and G. Branstator, 2011: Tropical–extratropical teleconnections in boreal summer: Observed interannual variability. *J. Climate*, **24**, 1878–1896, <https://doi.org/10.1175/2011JCLI3621.1>.
- Duchon, C. E., 1979: Lanczos filtering in one and two dimensions. *J. Appl. Meteor.*, **18**, 1016–1022, [https://doi.org/10.1175/1520-0450\(1979\)018<1016:LFIQAT>2.0.CO;2](https://doi.org/10.1175/1520-0450(1979)018<1016:LFIQAT>2.0.CO;2).
- Enomoto, T., 2004: Interannual variability of the Bonin high associated with the propagation of Rossby waves along the Asian jet. *J. Meteor. Soc. Japan*, **82**, 1019–1034, <https://doi.org/10.2151/jmsj.2004.1019>.
- , B. J. Hoskins, and Y. Matsuda, 2003: The formation mechanism of the Bonin high in August. *Quart. J. Roy. Meteor. Soc.*, **129**, 157–178, <https://doi.org/10.1256/qj.01.211>.
- Good, S. A., M. J. Martin, and N. A. Rayner, 2013: EN4: Quality controlled ocean temperature and salinity profiles and monthly objective analyses with uncertainty estimates. *J. Geophys. Res. Oceans*, **118**, 6704–6716, <https://doi.org/10.1002/2013JC009067>.
- Goswami, B. N., M. S. Madhusoodanan, C. P. Neema, and D. Sengupta, 2006: A physical mechanism for North Atlantic SST influence on the Indian summer monsoon. *Geophys. Res. Lett.*, **33**, L02706, <https://doi.org/10.1029/2005GL024803>.
- Hirons, L. C., N. P. Klingaman, and S. J. Woolnough, 2015: MetUM-GOML1: A near-globally coupled atmosphere–ocean–mixed-layer model. *Geosci. Model Dev.*, **8**, 363–379, <https://doi.org/10.5194/gmd-8-363-2015>.
- Hong, X., and R. Lu, 2016: The meridional displacement of the summer Asian jet, Silk Road Pattern, and tropical SST anomalies. *J. Climate*, **29**, 3753–3766, <https://doi.org/10.1175/JCLI-D-15-0541.1>.
- , —, and S. Li, 2017: Amplified summer warming in Europe–west Asia and northeast Asia after the mid-1990s. *Environ. Res. Lett.*, **12**, 094007, <https://doi.org/10.1088/1748-9326/aa7909>.
- Huang, G., Y. Li, and R. Huang, 2011: The interannual variability of summer rainfall in the arid and semiarid regions of northern China and its association with the Northern Hemisphere circumglobal teleconnection. *Adv. Atmos. Sci.*, **28**, 257–268, <https://doi.org/10.1007/s00376-010-9225-x>.
- Huang, W., J. H. Chen, X. J. Zhang, S. Feng, and F. H. Chen, 2015: Definition of the core zone of the “westerlies-dominated climatic regime”, and its controlling factors during the instrumental period. *Sci. China Earth Sci.*, **58**, 676–684, <https://doi.org/10.1007/s11430-015-5057-y>.
- Joshi, M. K., and A. Rai, 2015: Combined interplay of the Atlantic multidecadal oscillation and the interdecadal Pacific oscillation on rainfall and its extremes over Indian subcontinent. *Climate Dyn.*, **44**, 3339–3359, <https://doi.org/10.1007/s00382-014-2333-z>.

- Kiehl, J. T., J. J. Hack, G. Bonan, B. A. Boville, D. Williamson, and P. Rasch, 1998: The National Center for Atmospheric Research Community Climate Model: CCM3. *J. Climate*, **11**, 1131–1149, [https://doi.org/10.1175/1520-0442\(1998\)011<1131:TNCFAR>2.0.CO;2](https://doi.org/10.1175/1520-0442(1998)011<1131:TNCFAR>2.0.CO;2).
- Kosaka, Y., H. Nakamura, M. Watanabe, and M. Kimoto, 2009: Analysis on the dynamics of a wave-like teleconnection pattern along the summertime Asian jet based on a reanalysis dataset and climate model simulations. *J. Meteor. Soc. Japan*, **87**, 561–580, <https://doi.org/10.2151/jmsj.87.561>.
- , J. S. Chowdary, S. Xie, Y. Min, and J. Lee, 2012: Limitations of seasonal predictability for summer climate over East Asia and the northwestern Pacific. *J. Climate*, **25**, 7574–7589, <https://doi.org/10.1175/JCLI-D-12-00009.1>.
- , S.-P. Xie, N.-C. Lau, and G. A. Vecchi, 2013: Origin of seasonal predictability for summer climate over the northwestern Pacific. *Proc. Natl. Acad. Sci. USA*, **110**, 7574–7579, <https://doi.org/10.1073/pnas.1215582110>.
- Kretschmer, M., D. Coumou, J. F. Donges, and J. Runge, 2016: Using causal effect networks to analyze different Arctic drivers of midlatitude winter circulation. *J. Climate*, **29**, 4069–4081, <https://doi.org/10.1175/JCLI-D-15-0654.1>.
- Krishnamurti, T. N., A. K. Mishra, A. Simon, and A. Yatagai, 2009: Use of a dense rain-gauge network over India for improving blended TRMM products and downscaled weather models. *J. Meteor. Soc. Japan*, **87A**, 393–412, <https://doi.org/10.2151/jmsj.87A.393>.
- Krishnan, R., and M. Sugi, 2003: Pacific decadal oscillation and variability of the Indian summer monsoon rainfall. *Climate Dyn.*, **21**, 233–242, <https://doi.org/10.1007/s00382-003-0330-8>.
- Kumar, K. K., M. Hoerling, and B. Rajagopalan, 2005: Advancing dynamical prediction of Indian monsoon rainfall. *Geophys. Res. Lett.*, **32**, L08704, <https://doi.org/10.1029/2004GL021979>.
- Lau, W. K., and K. Kim, 2012: The 2010 Pakistan flood and Russian heat wave: Teleconnection of hydrometeorological extremes. *J. Hydrometeorol.*, **13**, 392–403, <https://doi.org/10.1175/JHM-D-11-016.1>.
- Lee, J.-Y., and Coauthors, 2010: How are seasonal prediction skills related to models' performance on mean state and annual cycle? *Climate Dyn.*, **35**, 267–283, <https://doi.org/10.1007/s00382-010-0857-4>.
- Lin, H., 2009: Global extratropical response to diabatic heating variability of the Asian summer monsoon. *J. Atmos. Sci.*, **66**, 2697–2713, <https://doi.org/10.1175/2009JAS3008.1>.
- , J. Derome, and G. Brunet, 2007: The nonlinear transient atmospheric response to tropical forcing. *J. Climate*, **20**, 5642–5665, <https://doi.org/10.1175/2007JCLI1383.1>.
- Lu, R.-Y., J.-H. Oh, and B.-J. Kim, 2002: A teleconnection pattern in upper-level meridional wind over the North African and Eurasian continent in summer. *Tellus*, **54A**, 44–55, <https://doi.org/10.3402/tellusa.v54i1.12122>.
- Neale, R. B., J. H. Richter, and M. Jochum, 2008: The impact of convection on ENSO: From a delayed oscillator to a series of events. *J. Climate*, **21**, 5904–5924, <https://doi.org/10.1175/2008JCLI2244.1>.
- Piao, J., W. Chen, K. Wei, Y. Liu, H. F. Graf, J.-B. Ahn, and A. Pogoreltsev, 2017: An abrupt rainfall decrease over the Asian inland plateau region around 1999 and the possible underlying mechanism. *Adv. Atmos. Sci.*, **34**, 456–468, <https://doi.org/10.1007/s00376-016-6136-5>.
- Poli, P., and Coauthors, 2016: ERA-20C: An atmospheric reanalysis of the twentieth century. *J. Climate*, **29**, 4083–4097, <https://doi.org/10.1175/JCLI-D-15-0556.1>.
- Rajeevan, M., and J. Bhate, 2009: A high resolution daily gridded rainfall dataset (1971–2005) for mesoscale meteorological studies. *Curr. Sci.*, **96**, 558–562.
- Rayner, N. A., D. E. Parker, E. B. Horton, C. K. Folland, L. V. Alexander, D. P. Rowell, E. C. Kent, and A. Kaplan, 2003: Global analyses of sea surface temperature, sea ice, and night marine air temperature since the late nineteenth century. *J. Geophys. Res.*, **108**, 4407, <https://doi.org/10.1029/2002JD002670>.
- Rodwell, M. J., and B. J. Hoskins, 1996: Monsoons and the dynamics of deserts. *Quart. J. Roy. Meteor. Soc.*, **122**, 1385–1404, <https://doi.org/10.1002/qj.49712253408>.
- Runge, J., V. Petoukhov, and J. Kurths, 2014: Quantifying the strength and delay of climatic interactions: The ambiguities of cross correlation and a novel measure based on graphical models. *J. Climate*, **27**, 720–739, <https://doi.org/10.1175/JCLI-D-13-00159.1>.
- , and Coauthors, 2015: Identifying causal gateways and mediators in complex spatio-temporal systems. *Nat. Commun.*, **6**, 8502, <https://doi.org/10.1038/ncomms9502>.
- Saeed, S., W. A. Müller, S. Hagemann, and D. Jacob, 2011: Circumglobal wave train and the summer monsoon over northwestern India and Pakistan: The explicit role of the surface heat low. *Climate Dyn.*, **37**, 1045–1060, <https://doi.org/10.1007/s00382-010-0888-x>.
- , N. V. Lipzig, W. A. Müller, F. Saeed, and D. Zanchettin, 2014: Influence of the circumglobal wave-train on European summer precipitation. *Climate Dyn.*, **43**, 503–515, <https://doi.org/10.1007/s00382-013-1871-0>.
- Sato, N., and M. Takahashi, 2006: Dynamical processes related to the appearance of quasi-stationary waves on the subtropical jet in the midsummer Northern Hemisphere. *J. Climate*, **19**, 1531–1544, <https://doi.org/10.1175/JCLI3697.1>.
- Schleussner, C. F., J. Runge, J. Lehmann, and A. Levermann, 2014: The role of the North Atlantic overturning and deep ocean for multi-decadal global-mean-temperature variability. *Earth Syst. Dyn.*, **5**, 103–115, <https://doi.org/10.5194/esd-5-103-2014>.
- Schubert, S., and Coauthors, 2009: A U.S. CLIVAR project to assess and compare the responses of global climate models to drought-related SST forcing patterns: Overview and results. *J. Climate*, **22**, 5251–5272, <https://doi.org/10.1175/2009JCLI3060.1>.
- Si, D., and Y. Ding, 2016: Oceanic forcings of the interdecadal variability in East Asian summer rainfall. *J. Climate*, **29**, 7633–7649, <https://doi.org/10.1175/JCLI-D-15-0792.1>.
- Stephan, C. C., Y. H. Ng, and N. P. Klingaman, 2018a: On Northern Hemisphere wave patterns associated with winter rainfall events in China. *Adv. Atmos. Sci.*, **35**, 1021–1034, <https://doi.org/10.1007/s00376-018-7267-7>.
- , N. P. Klingaman, P. L. Vidale, A. G. Turner, M.-E. Demory, and L. Guo, 2018b: Interannual rainfall variability over China in the MetUM GA6 and GC2 configurations. *Geosci. Model Dev.*, **11**, 1823–1847, <https://doi.org/10.5194/gmd-11-1823-2018>.
- Thorne, P. W., and R. S. Vose, 2010: Reanalyses suitable for characterizing long-term trends. *Bull. Amer. Meteor. Soc.*, **91**, 353–362, <https://doi.org/10.1175/2009BAMS2858.1>.
- Tyrllis, E., J. Lelieveld, and B. Steil, 2013: The summer circulation over the eastern Mediterranean and the Middle East: Influence of the South Asian monsoon. *Climate Dyn.*, **40**, 1103–1123, <https://doi.org/10.1007/s00382-012-1528-4>.
- Vellore, R. K., and Coauthors, 2016: Monsoon–extratropical circulation interactions in Himalayan extreme rainfall.

- Climate Dyn.*, **46**, 3517–3546, <https://doi.org/10.1007/s00382-015-2784-x>.
- Walters, D., and Coauthors, 2017: The Met Office Unified Model Global Atmosphere 6.0/6.1 and JULES Global Land 6.0/6.1 configurations. *Geosci. Model Dev.*, **10**, 1487–1520, <https://doi.org/10.5194/gmd-10-1487-2017>.
- Wang, B., and Coauthors, 2009: Advance and prospectus of seasonal prediction: Assessment of the APCC/CliPAS 14-model ensemble retrospective seasonal prediction (1980–2004). *Climate Dyn.*, **33**, 93–117, <https://doi.org/10.1007/s00382-008-0460-0>.
- Wang, L., P. Xu, W. Chen, and Y. Liu, 2017: Interdecadal variations of the Silk Road Pattern. *J. Climate*, **30**, 9915–9932, <https://doi.org/10.1175/JCLI-D-17-0340.1>.
- Williams, K. D., and Coauthors, 2015: The Met Office Global Coupled model 2.0 (GC2) configuration. *Geosci. Model Dev.*, **8**, 1509–1524, <https://doi.org/10.5194/gmd-8-1509-2015>.
- Willmott, C. J., and K. Matsuura, 2001: Terrestrial air temperature and precipitation: Monthly and annual time series (1950–1999). http://climate.geog.udel.edu/~climate/html_pages/README.ghcn_ts2.html.
- Wu, R., 2002: A mid-latitude Asian circulation anomaly pattern in boreal summer and its connection with the Indian and East Asian summer monsoons. *Int. J. Climatol.*, **22**, 1879–1895, <https://doi.org/10.1002/joc.845>.
- Yang, R., Z. Xie, and J. Cao, 2017: A dynamic index for the westward ridge point variability of the western Pacific subtropical high during summer. *J. Climate*, **30**, 3325–3341, <https://doi.org/10.1175/JCLI-D-16-0434.1>.
- Yasui, S., and M. Watanabe, 2010: Forcing processes of the summertime circumglobal teleconnection pattern in a dry AGCM. *J. Climate*, **23**, 2093–2114, <https://doi.org/10.1175/2009JCLI3323.1>.
- Yatagai, A., K. Kamiguchi, O. Arakawa, A. Hamada, N. Yasutomi, and A. Kito, 2012: APHRODITE: Constructing a long-term daily gridded precipitation dataset for Asia based on a dense network of rain gauges. *Bull. Amer. Meteor. Soc.*, **93**, 1401–1415, <https://doi.org/10.1175/BAMS-D-11-00122.1>.
- Zhang, Q., Y. Guan, and H. Yang, 2008: ENSO amplitude change in observation and coupled models. *Adv. Atmos. Sci.*, **25**, 361–366, <https://doi.org/10.1007/s00376-008-0361-5>.
- Zhu, Y., H. Wang, W. Zhou, and J. Ma, 2011: Recent changes in the summer precipitation pattern in East China and the background circulation. *Climate Dyn.*, **36**, 1463–1473, <https://doi.org/10.1007/s00382-010-0852-9>.